Research Article

# Dielectric and optical properties of Ni-doped $LaFeO_3$ nanoparticles

M. A. Matin[1] · M. N. Hossain[1] · M. M. Rhaman[1] · F. A. Mozahid[1] · M. A. Ali[2] · M. A. Hakim[1] · M. F. Islam[1]

Received: 4 July 2019 / Accepted: 7 October 2019 / Published online: 24 October 2019


**Abstract**
Un-doped and Ni-doped lanthanum ferrite nanoparticles were synthesized by solid-state method. Ni concentration-dependent structural, dielectric and optical properties of synthesized nanoparticles were investigated. X-ray diffraction patterns confirmed predominant single-phase orthorhombic crystal structure with space group Pbnm in all samples. Average crystallite size was found to vary from 19 to 21 nm with Ni concentration. The field emission scanning electron microscopy revealed nanocrystalline structure with homogenous distribution of particles. UV–Vis–NIR diffuse spectra captured at room temperature indicate that $La_{1-x}Ni_xFeO_3$ is an indirect band gap material. The band gap varies from 1.70 to 1.85 eV with changing Ni concentration. Frequency-dependent dielectric constant, dielectric loss and ac conductivity were studied at room temperature. The dielectric constant was found to increase with increasing Ni content at high frequency. The loss factor resulted from domain wall resonance exhibited an identical dispersion behavior of dielectric constant. At high frequencies, the dielectric losses of orthoferrites were found to be low. This is attributed to the restricted motion of domain wall pointing its plausible practical applications in magnetically tunable filters and oscillators.

**Keywords** Solid-state method · Nanocrystalline $LaFeO_3$ · Orthoferrites · Dielectric properties · Optical properties · Band gap

## 1 Introduction

Ferrites are a class of ceramic materials consisting of mixtures of various metal oxides. It finds many potential applications in the modern world [1–4]. Nowadays, a significant attention has been given to lanthanum ferrites ($LaFeO_3$) due to its exchange bias, opto-magnetic and multiferroic properties. These ferrites are candidates for memory devices, low power-consuming spintronic devices, oxygen permeation membranes, opto-magnetic sensors and electrode material in solid oxide fuel cells (SOFCs) [5, 6]. Manikandan et al. [7–10] also reported pure and doped ferrite nanomaterials for different applications such as photocatalyst for the degradation of dyes, catalytic oxidation of alcohols, antibacterial activity and sensor materials.

The rare-earth-based orthoferrites, $RFeO_3$ (R denotes rare-earth element), are orthorhombically distorted perovskites with four formula units per unit cell. In this structure, $Fe^{3+}$ occupies the orthorhombic site and $R^{3+}$ situates on the twofold axis [11–13, 13–19].

The orthorhombic structure of $LaFeO_3$ belongs to Pbnm space group displaying p-type semiconductor. It is an attractive electroceramics due to mixed ionic/electronic conductivity and chemical stability at high temperature [20]. It exhibits antiferromagnetic phenomena with Neel temperature ($T_N$) at 750 K [21]. Neutron diffraction studies on model $LaFeO_3$ proved that each $Fe^{3+}$ ion is confined to six(6) $Fe^{3+}$ ions with spins pair antiparallel [22]. Recently, ferromagnetism has also been reported for LFO nanoparticles. The effects of length scale, shape and anisotropy prevailed

✉ M. A. Matin, mmatin@gce.buet.ac.bd | [1]Department of Glass and Ceramic Engineering, Bangladesh University of Engineering and Technology (BUET), Dhaka 1000, Bangladesh. [2]Department of Physics, Chittagong University of Engineering and Technology (CUET), Chattogram 4349, Bangladesh.

at surface which shows the magnetization increased with decreasing particle size [23–25].

Significant research efforts are being made to search for new class of oxide materials with smaller band gaps to enhance visible light absorption. The doping at La and/or Fe site of $LaFeO_3$ conducted by researchers is shown to display significant effects on many properties of $LaFeO_3$. Some investigations have been reported for LFO bulk ceramics [26–36]. Improved dielectric and optical properties of doped LFO are important for its practical applications. In this context, for the first time we thoroughly investigated the effect of Ni doping on the structural, dielectric and optical properties of $LaFeO_3$ nanoparticles. $La_{1-x}Ni_xFeO_3$ ($x$: 0.0, 0.10 and 0.20) nanoparticles were synthesized with the variation in Ni doping level by solid-state reaction technique.

## 2 Experimental techniques

$La_{1-x}Ni_xFeO_3$ ($x$ = 0.0, 0.10 and 0.20) nanoparticles were synthesized by a solid-state reaction technique. The analytical-grade base materials, namely $La_2O_3$, NiO and $\gamma$-$Fe_2O_3$, were taken in stoichiometric proportion. Then, it was milled using in zirconia balls for 24 h to obtain homogeneous mixture. Next, calcination was carried out at 700 °C for 2 h followed by remilling in alcoholic media for 10 h. Next, the suspensions were dried at 120 °C. Then, obtained powders were pressed into disk-shaped samples of 15 mm in diameter under a compressive force of 40 kN. The pressed pellets were sintered at 750 °C for 2 h embedded in corresponding powders to avoid volatilization. The phase structure of the sintered powders was determined by X-ray diffractometry (XRD; PANalytical Empyrean). The microstructure of the polished samples was investigated by scanning electron microscopy (JSM-7600F, JEOL). For dielectric measurement, the sintered samples were properly flattened to obtain parallel and smooth surfaces. Then, a silver paste (SPI Flash-Dry Silver Paint) was applied on both polished surfaces and dried at 250 °C for 4 h to provide connection of electrodes. Dielectric property measurement was conducted by a precision impedance analyzer (6500B, Wayne Kerr Electronics, UK) at ambient condition at frequency ranging from 10 Hz to 100 MHz. Optical properties were measured by UV–VIS–NIR spectrometry (Lambda-1050, PerkinElmer, USA).

## 3 Results and discussion

### 3.1 X-ray diffraction

X-ray diffraction (XRD) patterns were captured at Bragg angle (2$\theta$) ranging from 20° to 80°. Figure 1 shows room temperature XRD patterns of $La_{1-x}Ni_xFeO_3$ ($x$ = 0.0, 0.10 and 0.20) samples. The peak intensity was shown to modulate with Ni content compared to pure $LaFeO_3$. However, all samples were shown to confirm single-phase orthorhombic crystal structure with Pbnm space group.

Evidently, a small trace of secondary phase $\gamma$-$Fe_2O_3$ was found to present in XRD patterns of both pure and Ni-doped samples. However, the apparently unavoidable formation of secondary phases during the synthesis of $LaFeO_3$-based materials has been reported in several articles [37, 38].

Obtained patterns were also further analyzed by the Rietveld refinement using Xpert HighScore plus with ICDD database. The crystallite size and strain are presented in Table 1. Average crystallite size was found to vary from 19 to 21 nm with the variation in Ni dopant level.

The ionic radius (0.69 A) of $Ni^{2+}$ is much less than the ionic radius (1.03 A) of $La^{3+}$ [39]. Thus, a significant strain is generated in parent LFO, which is found to be increased with $Ni^{2+}$ content concomitant with the Rietveld refinement strain data as shown in Table 1. Crystallite size was found to decrease with increasing $Ni^{2+}$ doping concentration. Similar result was reported for Ni-doped $BiFeO_3$ [40]. In contrast, with increasing $Ni^{2+}$ doping concentration crystallite size was shown to increase in $ZnFe_2O_4$ [10, 41–44]. In this context, we postulate that the initial crystal structure of parent material might play an important role. However, it is established through density functional theory (DFT) calculations that $Mn^{2+}$, $Co^{2+}$, $Ni^{2+}$ and $Cu^{2+}$ are both the A- and B-site dopants [45]. $Ca^{2+}$, $Sr^{2+}$, $Ba^{2+}$ and $Fe^{2+}$ are found to be A-site and

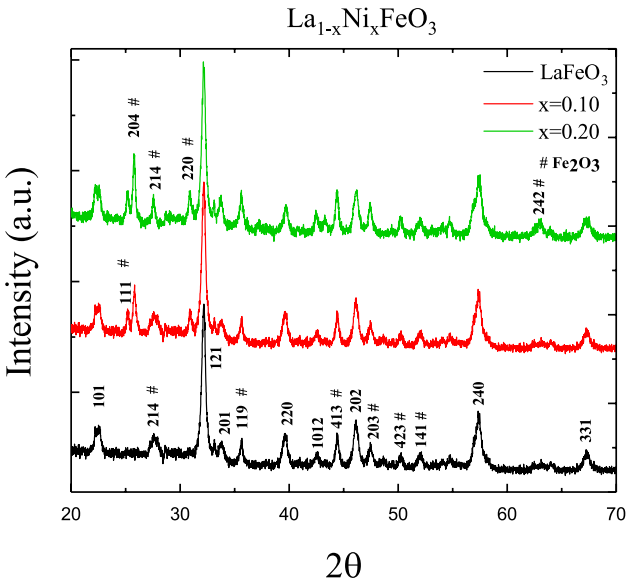


**Fig. 1** X-ray diffraction (XRD) patterns of $La_{1-x}Ni_xFeO_3$ ($x$ = 0, 0.1, 0.2) samples

**Table 1** Crystal parameters, crystallite size and lattice strain of LFO and Ni-doped LFO

| Samples ($La_{1-x}Ni_xFeO_3$) | Crystal parameters (Å) | Volume (Å$^3$) | $D$ (nm) | $\epsilon$ (%) | GOF |
|---|---|---|---|---|---|
| $x = 0.0$ | $a = 5.58803$, $b = 7.84259$, $c = 5.54317$ | 242.9274 | 20.7 | 0.607 | 1.90 |
| $x = 0.1$ | $a = 5.6177$, $b = 7.85131$, $c = 5.54495$ | 244.5712 | 19.6 | 0.641 | 2.30 |
| $x = 0.2$ | $a = 5.61863$, $b = 7.85281$, $c = 5.55731$ | 245.2309 | 18.9 | 0.663 | 2.63 |

$D$, crystallite size, $\epsilon$, lattice strain; GOF, goodness of fitting

$Mg^{2+}$ is considered to be B-site dopants. We doped $Ni^{2+}$ to substitute A-site $La^{3+}$ ion, but the increase in cell parameters and the volume of unit cell obtained from Rietveld analysis contradicts with our initial prediction. Thus, we postulate that that $Ni^{2+}$ substitutes B-site $Fe^{3+}$ ion of radius 0.55 A which demonstrates a good agreement with observed cell expansion and may rule out the possibility of the A-site substitution by $Ni^{2+}$ dopant.

### 3.2 Scanning electron microscopy

Shown in Fig. 2 are the scanning electron micrographs of the polished samples of $La_{1-x}Ni_xFeO_3$ ($x = 0, 0.1, 0.2$) nanoparticles which were calcined at 700 °C for 2 h. Evidently, all micrographs exhibit irregular particle shapes with a wide range of particle size distribution. The mean particle size of $La_{1-x}Ni_xFeO_3$ ($x = 0, 0.1, 0.2$) ceramics decreases with increasing Ni content. That means Ni doping was found to suppress grain growth. Inhibition of grain growth was also

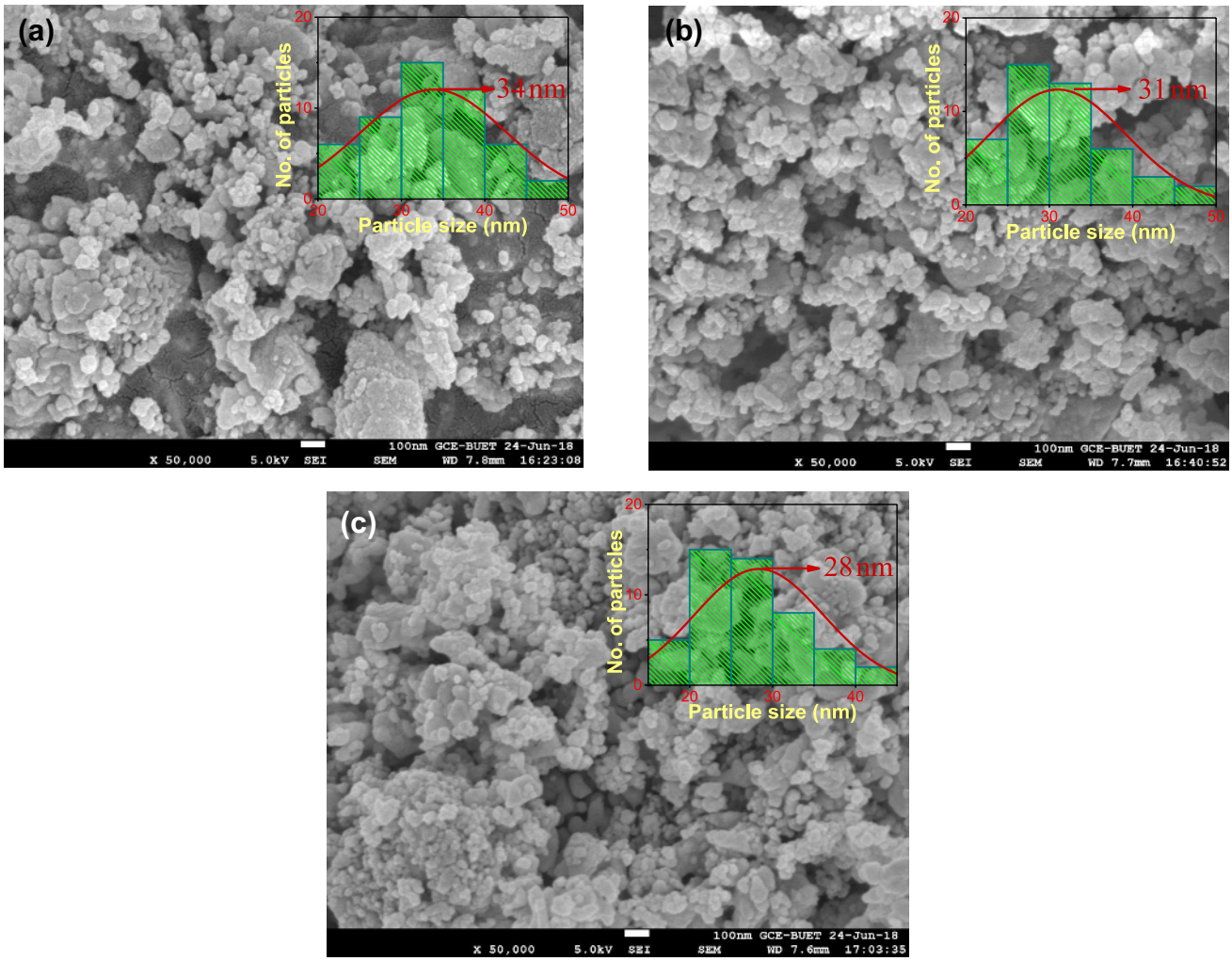


**Fig. 2** FESEM micrographs of $La_{1-x}Ni_xFeO_3$: **a** $x = 0.0$, **b** $x = 0.10$ and **c** $x = 0.20$

reported for Ni-doped $BiFeO_3$ [40]. The decreasing grain size of Ni-doped LFO can be resulted from the suppression of $O_2$ vacancy concentration (the slower the $O_2$ ion movement, the smaller the grain growth rate) and due to the difference in ionic radius of $La^{3+}$ and $Ni^{3+}$ [46–48]. In addition, oxygen vacancies are presumably generated due to Ni doping in LFO resulting structural distortion with concurrent reduction in crystallinity hence reducing the grain size.

However, during calcining the compositions at 700 °C high surface energy leads to neck formation by diffusion in solid state and nanoparticles agglomerate by the process of evaporation–condensation. In addition, both the particle size and crystal size of Ni-doped LFO nanoparticles reduce with increasing Ni content demonstrating the retardation of grain growth.

### 3.3 Dielectric properties

The room temperature measurement of dielectric behavior is presented in Fig. 3. Figure 3a shows how the dielectric constant varies with frequency ($10^2$–$10^7$ Hz). The increase in dielectric constant at low frequency is remarkable. The frequency regions may be subdivided into three regimes: (I) the first region (up to 103 Hz) in which the dielectric constant sharply decreases with frequency, (II) the region in which the dielectric constant decreases comparatively

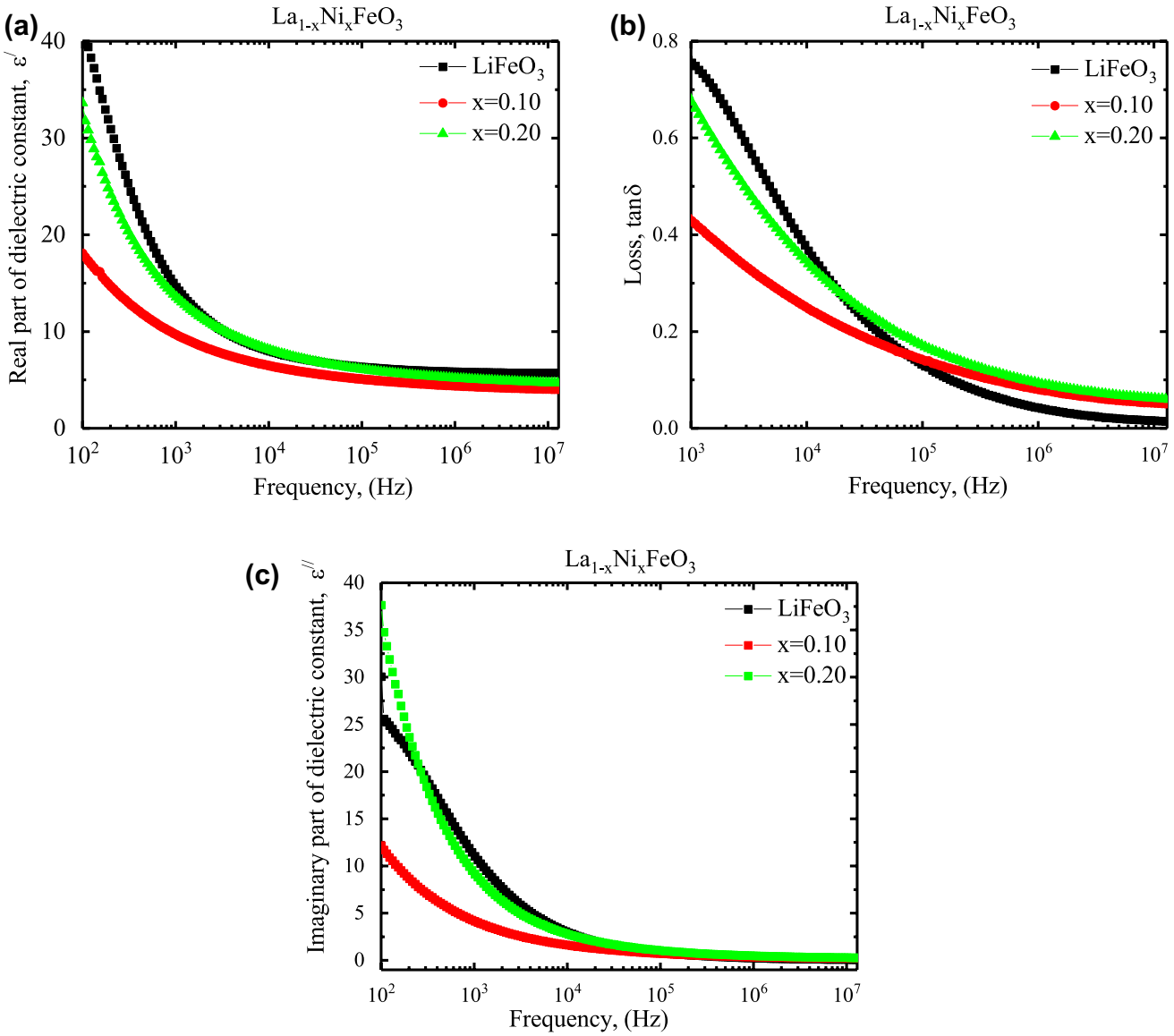


**Fig. 3** Frequency dependency of $La_{1-x}Ni_xFeO_3$ ($x$ = 0.1, 0.2) recorded at RT in the wide frequency range from 100 Hz to 120 MHz: **a** real part of the dielectric constant ($\epsilon'$), **b** imaginary part of the dielectric constant ($\epsilon''$) and **c** tangent losses (tan $\delta$)

slowly with frequency and (III) the frequency region in which the dielectric constant remains almost constant.

Similar type of dielectric behavior has also been observed in our investigated other dielectric materials [49, 50] and may be exemplified by polarization mechanism. At low frequencies, the dielectric constant is attributed to all types of polarization mechanisms and the contribution from various types of polarizations start to decrease with the increase in frequency. The dipolar including interfacial polarizations play role to dielectric constant at low frequencies. Basically, $Fe^{3+}/Fe^{2+}$ ions bring about dipolarity in ferrites. The electron exchange between these ions results the dipolar polarization, and the dipole alignment takes place by AC field. After a certain frequency of AC field, the dipolar polarization does not contribute to the dielectric constant. This is because the electron exchange between $Fe^{2+}$ and $Fe^{3+}$ cannot follow alternating field. The dielectric constant is attributed only to the electronic polarization at very high-frequency region [51]. The electronic polarization is independent on frequency, resulting in a constant value of dielectric constant at high frequency. The effect of trace secondary phase may also be noted. The dielectric dispersion of $\gamma$-$Fe_2O_3$ was absent after annealing above 550 °C [52]. Thus, the observed dielectric behavior of LFO was not expected to alter remarkably.

The lagging in the polarization with respect to the AC field can be represented by the dielectric loss (tan$\delta$). Figure 3b shows the frequency dependence of tan$\delta$ for $La_{1-x}Ni_xFeO_3$ system where no loss peak is observed. The nonexistence of any peak in tan$\delta$ defines the system as charge carrier-dominated system where the dominant contribution to polarization stems from electronic or ionic charges [53]. The similar type of behavior was also observed for $EuFeO_3$ [51].

### 3.4 AC conductivity

With the purpose of further studying the transport mechanism, the AC conductivity at different Ni contents is investigated. Figure 4 presents the frequency-dependent conductivity for different doping concentrations at room temperature. A plateau regime was observed at lower frequency while a dispersion region was found at higher frequency.

The Maxwell–Wagner two layers formalism can be applied to the observed phenomenon [54]. The plateau region characterizes the dc conductivity. The frequency-independent conductivity may be attributed to the random diffusion by activated hopping of ionic charge carriers. Therefore, the conductivity can be described by Jonscher's universal power law [55]

$$\sigma_{ac}(\omega) = \sigma_{dc} + D\omega^{s} \quad (1)$$

where the first part ($\sigma_{dc}$) of right-hand side is defined as the dc conductivity and the left part of the above equation is the frequency-dependent conductivity [56]. The frequency exponent '$s$' has the value in the range of $0 < s < 1$ while the of $s$ is 1 suggesting an ideal Debye-type behavior. The value of s can be calculated from the $\log\sigma_{ac}$ versus $\log\omega$, and the calculated values are 0.55, 0.71, 0.65 for $x = 0.0$, 0.10 and 0.20, respectively.

A hopping mechanism for the direct current electrical conductivity is associated with a small value of activation energy. The small polaron can migrate by thermal activation from $Fe^{2+}$ to $Fe^{3+}$ sites contributing to the change in

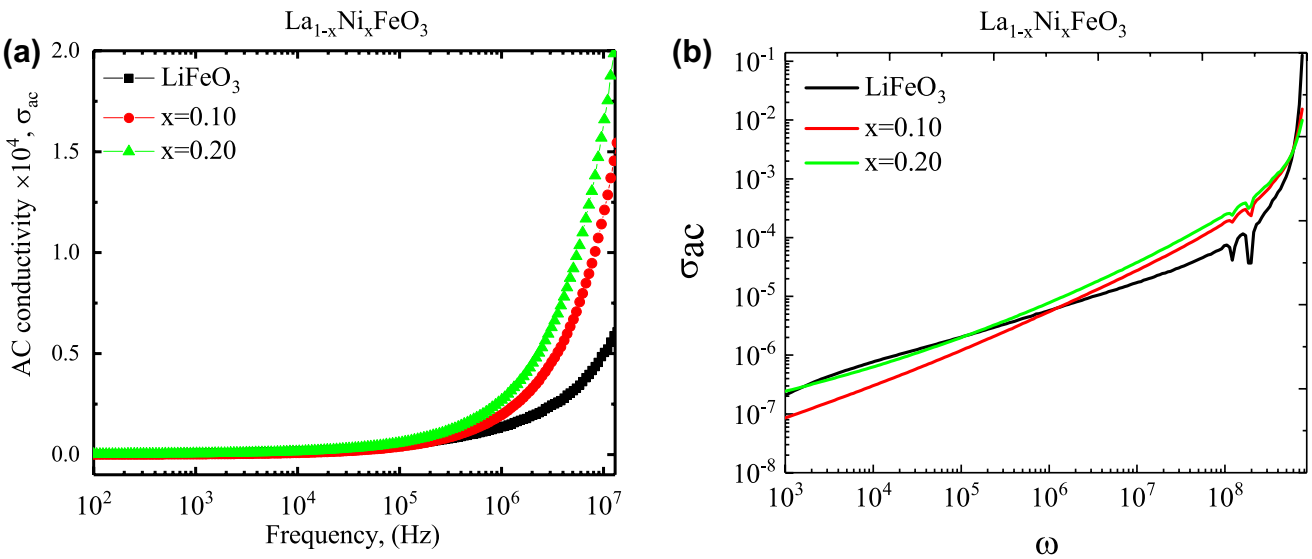


**Fig. 4** **a** Frequency dependence of AC conductivity for $La_{1-x}Ni_xFeO_3$ ($x = 0$, 0.1, 0.2) ceramic and **b** $\log\sigma_{ac}$ vs $\log\omega$

mobility. This phenomenon requires the reduction in a small fraction of $Fe^{3+}$ to $Fe^{2+}$ with a simultaneous creation of coordinated oxygen vacancy to satisfy the neutrality of a $\gamma$-$Fe_2O_3$ crystallite [57]. Thus, the effect of trace secondary phase would not significantly deteriorate the dc conductivity (ac conductivity at low frequencies) of parent LFO.

### 3.5 Band gap tuning

With small band gap energy, LFO is a plausible attractive visible light irradiator. The photovoltaic (pv) absorption capacity of LFO is correlated with its electronic structure and thereby major contributor to their band gaps [58]. In this context, the diffused reflectance spectra captured by UV–Vis–NIR spectrophotometry (PE-1050) were used to obtain band gap energy, $E_g$ of synthesized all nanomaterials. $E_g$ was calculated by applying Kubelka/Munk function defined as: $F(R) = (1-R)^2/2R$, where R is the diffused reflectance. Shown in Fig. 5 are $[F(R)h\nu]^2$ versus $h\nu$ graphs.

$E_g$ is obtained from the plots by drawing tangent lines at upper linear part of the curves. The point of intersection of a tangent at $[F(R)h\nu]^2 = 0$ is $E_g$ [59]. Basically, $E_g$ is the differentiate energy between (O:2*p*) valence band and (Fe:3*d*) conduction band of LFO. Table 2 summarizes obtained band gaps of pure LFO and Ni-doped LFO.

The observed reduction in $E_g$ may stem from many contributors. The Fe–O octahedral restructuring of molecular orbital can reduce $E_g$ [60]. The length scale of nanoparticles also affects the value of $E_g$ [61], i.e., $E_g$ scales with the size of particles. Theoretical calculation claimed that generation of new energy level between Fe:*3d* and O:*2p* by doping can reduce the effective $E_g$ of LFO [62]. In addition, the Ni content in LFO might change the Fe–O bond length and Fe–O–Fe bond angle resulting in impact on $E_g$ by modulating one-electron band width (*w*) [63]. $E_{cb}$ of $Ni^{2+}$ is – 4.39 eV, and $E_{cb}$ of $Fe^{2+}$ is – 4.33 eV; thus, $E_{cb}^{Ni} < E_{cb}^{Fe}$ [64] that may also reduce $E_g$. The experimental formula correlating *w* with bond length and bond angle reads

$$w = \frac{cos\omega}{d_{Fe-O}^{3.5}} \tag{2}$$

where $d_{Fe-O}$ is Fe–O bond length and

$$\omega = \frac{1}{2}(\pi - (\mathrm{Fe} - O - Fe)) \tag{3}$$

$E_g$ is linked to *w* by $E_g = \Pi$-w. Here, $\Pi$ is the energy related to charge transfer [65]. Thus, the increase in bond angle, Fe–O–Fe, and the reduction in bond length, $d_{Fe-O}$, by Ni doping resulted in the increase in the value of *w* and thus the reduction in $E_g$. However, the band gap of $\gamma$-$Fe_2O_3$ is reported to be 2.0–2.2 eV [66, 67]; thus, it would interfere negatively with the purpose of lowering the band gap of LFO by doping.

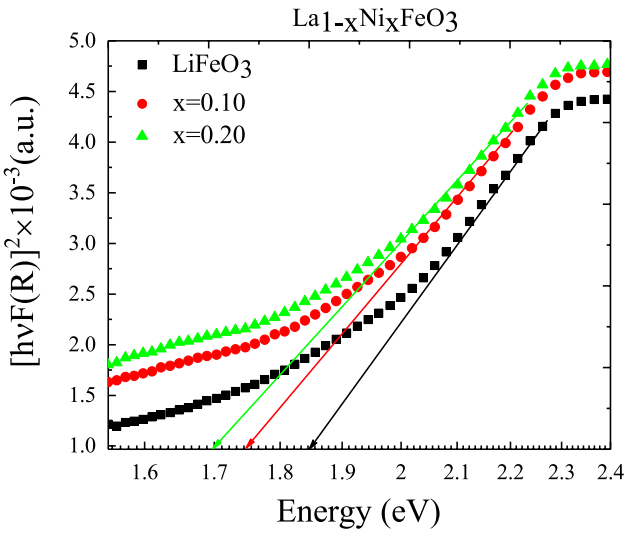


**Fig. 5** $[h\nu F(R)]^2$ versus $h\nu$ (photon energy, eV) plots to calculate band gap energy for Ni-doped LFO

**Table 2** Band gap, mean particle size and lattice strain of LFO and Ni-doped LFO

| Samples ($La_{1-x}Ni_xFeO_3$) | Band gap (eV) | Mean particle size (nm) |
|---|---|---|
| $x = 0.0$ | 1.85 | 34 |
| $x = 0.1$ | 1.75 | 31 |
| $x = 0.2$ | 1.70 | 28 |

## 4 Conclusions

Pure LFO and $La_{1-x}Ni_xFeO_3$ (Ni-doped LFO) nanoparticles were successfully synthesized by conventional solid-state method. The parent crystal structure of LFO was found to retain in doped LFO. The size of crystallite was shown to decrease with increasing Ni doping level. The concurrently induced lattice strain increased with the reduction in crystallite size. However, the presence of clusters cannot be ruled out within the scope of XRD and FESEM experimental techniques. A significant agglomeration effect was thus presumably present in all synthesized nanostructured samples as confirmed by the disagreement between the crystallite size estimated from XRD patterns and the particle size calculated from FESEM images. Ni doping in LFO enhances its optical properties. The optical band gap was shown to decrease to 1.70 eV with 20 (at.)% Ni doping. Higher values of dielectric constant were obtained at low frequencies due to the conduction mechanism of heterogeneous nature. The observed dispersion at low

frequencies may resulted from electronic polarization by the underlying hopping mechanism of polaron. The AC conductivity ($\sigma_{AC}$) was found to increase with increasing Ni concentration. When the frequency of the applied field increases, the conduction process might be affected by 3d hopping electrons between $Fe^{2+}/Fe^{3+}$ ions and $Ni^{2+}/Ni^{3+}$ ions. The improved properties of synthesized Ni-doped LFO provide a scientific implication for its plausible applications in magnetically tunable filters and oscillators.

**Acknowledgements** We highly acknowledge the permission of laboratory facilities at Multi-scale lab of the GCE Dept, BUET, Dhaka-1000.

## Compliance with ethical standards

**Conflict of interest** The authors declare that they have no conflict of interest.

## References

1. Abdellatif MH, Azab AA, Moustafa AM (2018) Dielectric spectroscopy of localized electrical charges in ferrite thin film. J Electron Mater 47:378–384
2. Tokunaga Y, Furukawa N, Sakai H, Taguchi Y, Arima TH, Tokura Y (2009) Composite domain walls in a multiferroic perovskite ferrite. Nat Mater 8:558
3. Habib Z, Majid K, Ikram M, Asokan K (2015) Structural analysis and dielectric properties of $HoFe_{1-x}Ni_xO_3$. J Electron Mater 44:1044–1053
4. Wang D, Gong M (2011) Surface and shape anisotropy effects in $LaFeO_3$ nanoparticles. J Appl Phys 109:114304
5. Naseem S, Khan S, Husain S, Khan W (2018) Exploring the room-temperature ferromagnetism and temperature-dependent dielectric properties of Sr/Ni-doped $LaFeO_3$ nanoparticles synthesized by reverse micelle method. J Electron Mater 47:1916–1923
6. Liu T, Xu Y (2011) Synthesis of nanocrystalline $LaFeO_3$ powders via glucose sol–gel route. Mater Chem Phys 129:1047–1050
7. Hema E, Manikandan A, Gayathri M, Durka M, Arul Antony S, Venkatraman BR (2016) The role of $Mn^{2+}$ doping on structural, morphological, optical, magnetic and catalytic properties of spinel $ZnFe_2O_4$ nanoparticles. J Nanosci Nanotechnol 16:5929–5943
8. Silambarasu A, Manikandan A, Balakrishnan K (2017) Room-temperature superparamagnetism and enhanced photocatalytic activity of magnetically reusable spinel $ZnFe_2O_4$ nanocatalysts. J Supercond Novel Magn 30:2631–2640
9. Sonia MML, Anand S, Vinosel VM, Janifer MA, Pauline S, Manikandan A (2018) Effect of lattice strain on structure, morphology and magneto-dielectric properties of spinel $NiGd_xFe_{2-x}O_4$ ferrite nano-crystallites synthesized by sol–gel route. J Magn Magn Mater 466:238–251
10. Elayakumar K, Dinesh A, Manikandan A, Palanivelu M, Kavitha G, Prakash S, Kumar RT, Jaganathan SK, Baykal A (2019) Structural, morphological, enhanced magnetic properties and antibacterial bio-medical activity of rare earth element (REE) Cerium ($Ce_{3+}$) doped $CoFe_2O_4$ nanoparticles. J Magn Magn Mater 476:157–165
11. Josephine BA, Manikandan A, Teresita VM, Antony SA (2016) Fundamental study of $LaMg_xCr_{1-x}O_{3-d}$ perovskites nano-photocatalysts: sol–gel synthesis, characterization and humidity sensing. Korean J Chem Eng 33:1590–1598
12. Teresita VM, Manikandan A, Josephine BA, Sujatha S, Antony SA (2016) Electromagnetic properties and humidity-sensing studies of magnetically recoverable $LaMg_xFe_{1-x}O_{3-\delta}$ perovskites nano-photocatalysts by sol–gel route. J Supercond Novel Magn 29:1691–1701
13. Rajmohan S, Manikandan A, Jeseentharani V, Antony SA, Pragasam J (2016) Simple co-precipitation synthesis and characterization studies of $La_{1-x}Ni_xVO_3$ perovskites nanostructures for humidity sensing applications. J Nanosci Nanotechnol 16:1650–1655
14. Ravichandran AT, Srinivas J, Karthick R, Manikandan A, Baykal A (2018) Facile combustion synthesis, structural, morphological, optical and antibacterial studies of $Bi_{1-x}Al_xFeO_3$ ($0.0 \geq x \leq 0.15$) nanoparticles. Ceram Int 44:13247–13252
15. White R (1969) Review of recent work on the magnetic and spectroscopic properties of the rare-earth orthoferrites. J Appl Phys 40:1061–1069
16. LeCraw RC, Wolfe R, Gyorgy EM, Hagedorn FB, Hensel JC, Remeika JP (1969) Microwave absorption near the reorientation temperature in rare earth orthoferrites. J Appl Phys 39:1019–1020
17. Park JH, Kimura T, Tokura Y (1998) Competition between lattice distortion and charge dynamics for the charge carriers of double-layered manganites. Phys Rev B 58:R13330
18. Yamaguchi T (1974) Theory of spin reorientation in rare-earth orthochromites and orthoferrites. J Phys Chem Solids 35:479–500
19. Forestier H, Guiot-Guillain G (1950) A new series of ferromagnetic bodies: the ferrites of rare earths. C R 230:1844
20. Yoon JW, Grilli ML, Bartolomeo ED, Polini R, Traversa E (2001) The $NO_2$ response of solid electrolyte sensors made using nano-sized $LaFeO_3$ electrodes. Sens Actuators B Chem 76:483–488
21. Falcon H, Goeta AE, Punte G, Carbonio RE (1997) Crystal structure refinement and stability of $LaFe_xNi_{1-x}O_3$ solid solutions. J Solid State Chem 133:379–385
22. Koehler WC, Wollan EO, Wilkinson MK (1960) Neutron diffraction study of the magnetic properties of rare-earth-iron perovskites. Phys Rev 118:58
23. Phokha S, Pinitsoontorn S, Rujirawat S, Maensiri S (2015) Polymer pyrolysis synthesis and magnetic properties of $LaFeO_3$ nanoparticles. Physica B 476:55–60
24. Qiu Y, Luo YS, Zou ZJ, Tian ZM, Yuan SL, Xi Y, Huang LZ (2014) Size effect on magnetic and dielectric properties in nanocrystalline $LaFeO_3$. J Mater Sci Mater Electron 25:760–764
25. Thuy NT, Minh DL (2012) Size effect on the structural and magnetic properties of nanosized perovskite $LaFeO_3$ prepared by different methods. Adv Mater Sci Eng 2012:380306. https://doi.org/10.1155/2012/380306
26. Shikha P, Kang TS, Randhawa BS (2015) Effect of different synthetic routes on the structural, morphological and magnetic properties of Ce doped $LaFeO_3$ nanoparticles. J Alloys Compd 625:336–345
27. Acharya S, Chakrabarti PK (2010) Some interesting observations on the magnetic and electric properties of $Al^{3+}$ doped lanthanum orthoferrite ($La_{0.5}Al_{0.5}FeO_3$). Solid State Commun 150:1234–1237
28. Selvadurai APB, Pazhanivelu V, Jagadeeshwaran C, Murugaraj R, Muthuselvam IP, Chou FC (2015) Influence of Cr substitution on structural, magnetic and electrical conductivity spectra of $LaFeO_3$. J Alloys Compd 646:924–931
29. Cao E, Qin Y, Cui T, Sun L, Hao W, Zhang Y (2017) Influence of Na doping on the magnetic properties of $LaFeO_3$ powders and dielectric properties of $LaFeO_3$ ceramics prepared by citric sol–gel method. Ceram Int 43:7922–7928
30. Phokha S, Hunpratup S, Pinitsoontorn S, Putasaeng B, Rujirawat S, Maensiri S (2015) Structure, magnetic, and dielectric

properties of Ti-doped $LaFeO_3$ ceramics synthesized by polymer pyrolysis method. Mater Res Bull 67:118–125
31. Saad AA, Khan W, Dhiman P, Naqvi AH, Singh M (2013) Structural, optical and magnetic properties of perovskite $(La_{1-x}Sr_x)(Fe_{1-x}Ni_x)O_3$, (x = 0.0, 0.1 and 0.2) nanoparticles. Electron Mater Lett 9:77–81
32. Bellakki MB, Kelly BJ, Manivannan V (2010) Synthesis, characterization, and property studies of (La, Ag)$FeO_3$ perovskites. J Alloys Compd 489:64–71
33. Bellakki MB, Manivannan V (2010) Solution combustion synthesis of (La, K)$FeO_3$ orthoferrite ceramics: structural and magnetic property studies. Bull Mater Sci 33:611–618
34. Troyanchuk IO, Karpinsky DV, Szymczak R, Szymczak H (2006) Effect of oxygen deficit on magnetic properties of $LaCo_{0.5}Fe_{0.5}O_3$. J Magn Magn Mater 298:19–24
35. Chandrasekhar KD, Mallesh S, Murthy JK, Das AK, Venimadhav A (2014) Role of defects and oxygen vacancies on dielectric and magnetic properties of $Pb^{2+}$ ion doped $LaFeO_3$ polycrystalline ceramics. Physica B 448:304–311
36. Manzoor S, Husain S (2018) Analysis of Zn substitution on structure, optical absorption, magnetization, and high temperature specific heat anomaly of the nanocrystalline $LaFeO_3$. J Appl Phys 124:065110
37. Gosavi PV, Biniwale RB (2010) Pure phase $LaFeO_3$ perovskite with improved surface area synthesized using different routes and its characterization. Mater Chem Phys 119:324–329
38. Aono H, Tomid M, Sadaoka Y (2009) Conventional synthesis method for fine polymetallic $LaFeO_3$ using ethylene glycol solvent addition. J Ceram Soc Jpn 117:1048–1051
39. Shannon RD (1976) Revised effective ionic radii and systematic studies of interatomie distances in halides and chaleogenides. Acta Crystallogr A32:751–767
40. Castaneda R, Aquino JAM, George GR, Silva J, Montero MEF, Rojas AR, Fuentes L (2013) Effects of Ni doping on ferroelectric and ferromagnetic properties of $Bi_{0.75}Ba_{0.25}FeO_3$. Ceram Int 39:8527–8530
41. Kumar A, Annveer, Arora M, Yadav MS, Pant RP (2010) Induced size effect on Ni doped nickel zinc ferrite nanoparticles. Phys Procedia 9:20–23
42. Rahimi H, Ghasemi A, Mozaffarinia R, Tavoosi M (2016) On the magnetic and structural properties of neodymium iron boron nanoparticles. J Supercond Novel Magn 29:2141–2149
43. Manikandan A, Durka M, Selvi MA, Antony SA (2016) Sesamum indicum plant extracted microwave combustion synthesis and opto-magnetic properties of spinel $Mn_xCo_{1-x}Al_2O_4$ nano-catalysts. J Nanosci Nanotechnol 16:448–456
44. Asiria S, Sertkol M, Guner S, Gungunes H, Batoo KM, Sozeri H, Saleh TA, Almessiere MA, Manikandan A, Baykal A (2018) Hydrothermal synthesis of $Co_yZn_yMn_{1-2y}Fe_2O_4$ nanoferrites: magneto-optical investigation. Ceram Int 44:5751–5759
45. Taylor FH, Buckeridge J, Catlow CRA (2017) Screening divalent metals for a- and b-site dopants in $LaFeO_3$. Chem Mater 29:8147–8157
46. Manikandan A, Durka M, Seevakan K, Antony SA (2015) A novel one-pot combustion synthesis and opto-magnetic properties of magnetically separable spinel $Mn_xMg_{1-x}Fe_2O_4$ ($0.0 \geq x \leq 0.5$) nanophotocatalysts. J Supercond Novel Magn 28:1405–1416
47. Manikandan A, Durka M, Antony SA (2014) A novel synthesis, structural, morphological, and opto-magnetic characterizations of magnetically separable spinel $Co_xMn_{1-x}Fe_2O_4$ ($0 \geq x \leq 1$) nano-catalysts. J Supercond Novel Magn 27:2841–2857
48. Hema E, Manikandan A, Karthika P, Antony SA, Venkatraman BR (2015) A novel synthesis of $Zn_{2+}$-doped $CoFe_2O_4$ spinel nanoparticles: structural, morphological, opto-magnetic and catalytic properties. J Supercond Novel Magn 28:2539–2552
49. Ali MA, Khan MNI, Chowdhury FUZ, Akhter S, Uddin MM (2015) Structural properties, impedance spectroscopy and dielectric spin relaxation of Ni–Zn ferrite synthesized by double sintering technique. J Sci Res 7:65
50. Ali MA, Uddin MM, Khan MNI, Chowdhury FUZ, Haque SM, Liba SI (2017) Magnetic properties of Sn-substituted Ni–Zn ferrite: synthesized from nano-sized powders of NiO, ZnO, $Fe_2O_3$ and $SnO_2$. J Magn Magn Mater 424:148–154
51. Sultan K, Ikrama M, Asokan K (2015) Effect of Mn doping on structural, morphological and dielectric properties of $EuFeO_3$ ceramics. RSC Adv 5:93867–93876
52. Iwauci K (1971) Dielectric properties of fine particles of $Fe_3O_4$ and some ferrites. Jpn J Appl Phys 10:1520–1528
53. Jonscher AK (1992) The universal dielectric response and its physical significance. IEEE Trans Electron Insul 27:407–423
54. Jonscher AK (1999) Dielectric relaxation in solids. J Phys D Appl Phys 32:57
55. Jonscher AK (1996) Universal relaxation law. Chelsea Dielectics Press, London
56. Matin MA, Hossain MN, Ali MA, Hakim MA, Islam MF (2019) Enhanced dielectricproperties of prospective $Bi_{0.85}Gd_{0.15}Fe_{1-x}Cr_xO_3$ multiferroics. Results Phys. https://doi.org/10.1016/j.rinp.2019.01.079
57. Nikumbh AK, Sayanekar PL, Chaskar MG (1991) Magnetic and electrical properties of γ-$Fe_2O_3$ prepared from ferrous malonate dihydrate. J Magn Magn Mater 97:119–125
58. Shen H, Cheng G, Wu A, Xu J, Zhao J (2009) Combustion synthesis and characterization of nano-crystalline $LaFeO_3$ powder. Physica Status Solidi 206:1420–1424
59. Kondo N, Itoh H, Kurihara M, Sakamoto M, Aono H, Sadaoka Y (2006) New high-yield preparation procedure of $Ln[Fe(CN)_6].nH_2O$ (Ln = La, Gd, and Lu) and their thermal decomposition into perovskite-type oxides. J Alloys Compd 408:1026–1029
60. Sivakumar M, Gedanken A, Zhong W, Jiang YH, Du YW, Brukental I, Nowik I (2004) Sonochemical synthesis of nanocrystalline $LaFeO_3$. J Mater Chem 14:764–769
61. Popa M, Frantti J, Kakihana M (2002) Lanthanum ferrite $LaFeO_3$ nanopowders obtained by the polymerizable complex method. Solid State Ion 154:437–445
62. Tiwari A, Mishra YK, Kobayashi H, Turner AP (eds) (2016) Intelligent nanomaterials. Wiley, Hoboken
63. Li K, Wang D, Wu F, Xie T, Li T (2000) Surface electronic states and photovoltage gas-sensitive characters of nanocrystalline $LaFeO_3$. Mater Chem Phys 64:269–272
64. Wang Y, Zhu J, Zhang L, Yang X, Lu L, Wang X (2006) Preparation and characterization of perovskite $LaFeO_3$ nanocrystals. Mater Lett 60:1767–1770
65. Kumar M, Srikanth S, Ravikumar B, Alex TC, Das SK (2009) Synthesis of pure and Sr-doped $LaGaO_3$, $LaFeO_3$ and $LaCoO_3$ and Sr, Mg-doped $LaGaO_3$ for ITSOFC application using different wet chemical routes. Mater Chem Phys 113:803–815
66. Bepari RA, Bharali P, Das BK (2017) Controlled synthesis of α- and γ-$Fe_2O_3$ nanoparticles via thermolysis of PVA gels and studies on α-$Fe_2O_3$ catalyzed styrene epoxidation. J Saudi Chem Soc 21:S170–S178
67. Chirita M, Grozescu I (2009) $Fe_2O_3$—nanoparticles, physical properties and their photochemical and photoelectrochemical applications. Chem Bull Politehnica Univ (Timisoara) 54:1–8